Eur. Phys. J. A (2018) **54**: 183
DOI 10.1140/epja/i2018-12619-x

The European Physical Journal A

Regular Article – Experimental Physics

Neutron inelastic scattering on ^{54}Fe

A. Olacel[1,a], C. Borcea[1], M. Boromiza[1,2], Ph. Dessagne[3], G. Henning[3], M. Kerveno[3], L. Leal[4], A. Negret[1], M. Nyman[5], and A.J.M. Plompen[5]

[1] Horia Hulubei National Institute for Physics and Nuclear Engineering, Reactorului 30, 077125 Bucharest-Măgurele, Romania
[2] University of Bucharest, Faculty of Physics, Atomistilor 405, 077125, Bucharest-Măgurele, Romania
[3] Université de Strasbourg, CNRS, IPHC UMR 7178, F - 67000 Strasbourg, France
[4] Institut de Radioprotection et de Sûreté Nucléaire, BP 17 - 92262 Fontenay-aux-Roses Cedex, France
[5] European Commission, Joint Research Centre, Retieseweg 111, B - 2440 Geel, Belgium

Received: 9 July 2018 / Revised: 17 September 2018

Communicated by A. Orbetelli

Abstract. A neutron inelastic scattering experiment was performed at the Geel Electron Linear Accelerator neutron source using an enriched ^{54}Fe sample. The γ rays produced in the reaction were detected using the Gamma Array for Inelastic Neutron Scattering spectrometer. For each observed transition we determined the γ-production cross section for incident energies ranging from the inelastic threshold ($\approx 1.434\,\mathrm{MeV}$) up to 18 MeV. Using these primary data we also calculated the cross section of the first excited level and the total inelastic cross section. Our experimental results are compared with previous reported values, evaluated nuclear data libraries and theoretical calculations performed with the TALYS 1.9 code. A careful tuning of the optical model parameters allowed significant improvements in the description of the experimental results leading to interesting conclusions regarding the interaction of the ^{54}Fe nucleus with neutrons.

1 Introduction

Inelastic neutron scattering is the predominant slowing-down mechanism for fast neutrons in a nuclear reactor, directly connected to the reactor multiplication factor (k_{eff}) and heat production. Because steel is present in large quantities as a structural material, accurate and precise experimental data on inelastic neutron scattering by iron nuclei are required for the evaluated libraries used in the design of nuclear facilities. During the recent years a major effort has been underway to provide better experimental data for improving reliability in criticality safety calculations for various applications including shipping casks, radiation dose prediction, reactor operation and shielding. The required uncertainty is typically below 5%.

Natural iron has four stable isotopes with the following natural abundances: ^{56}Fe [91.75(11)%], ^{54}Fe [5.85(11)%], ^{57}Fe [2.12(3)%] and ^{58}Fe [0.28(1)%] [1]. The Collaborative International Evaluated Library Organization Pilot Project (CIELO) [2,3], a subgroup of the Working Party on International Nuclear Data Evaluation Cooperation (WPEC) of the Nuclear Energy Agency focuses on the evaluation of the major isotope, ^{56}Fe [4]. The presence in the ^{56}Fe cross section of strong scattering resonances with deep interference minima enhances the importance of the minor isotopes as for certain neutron energies the scattering cross section of the minor isotopes dominates. In addition, the availability of a highly accurate and extensive cross section data set on ^{54}Fe allowed us to perform a detailed tuning of the theoretical calculations of relevance for this nuclear region by adjusting some of the parameters of the optical model potential used by the TALYS 1.9 code.

Our group started the measurement campaign on the stable isotopes of iron with cross section measurements of the $^{56}\mathrm{Fe}(\mathrm{n},\mathrm{n}'\gamma)$ reaction [5], followed by the $^{57}\mathrm{Fe}(\mathrm{n},\mathrm{n}'\gamma)$ reaction [6] and now $^{54}\mathrm{Fe}(\mathrm{n},\mathrm{n}'\gamma)$. The aim of these measurements is to produce precise and reliable data which will be further evaluated in order to generate nuclear data libraries. This task proved to be particularly difficult for the case of ^{57}Fe where the first transition could not be detected. Consequently, extensive theoretical calculations were performed for that case in order to complement the available experimental information. Unlike that situation, for ^{54}Fe the most important γ transitions were detected and hence dedicated calculations were done to achieve a better agreement between the experimental and theoretical values for the most intense transition.

The Exchange Format (EXFOR) data base [7,8] contains several previous γ-production cross sections, level

---

[a] e-mail: `aolacel@tandem.nipne.ro`

Table 1. Summary of previous experiments of neutron inelastic scattering on ^{54}Fe available in the EXFOR database.

Reference	Year	E_n range (MeV)	Method	Sample	EXFOR entry
Beghian *et al.* [9]	1955	2.50	γ spectroscopy	67.00% ^{54}Fe	21379
Broder *et al.* [10]	1962	2.00–3.96	γ spectroscopy	^{nat}Fe	40811
Benjamin *et al.* [11]	1967	3.00–5.25	γ spectroscopy	97.64% ^{54}Fe	11723
Jönsson *et al.* [12]	1969	15.00	γ spectroscopy	^{nat}Fe	20164
Breunlich *et al.* [13]	1971	14.40	γ spectroscopy	^{nat}Fe	21286
Boschung *et al.* [14]	1971	4.04–5.60	n spectroscopy	97.60% ^{54}Fe	10037
Kinney *et al.* [15]	1974	5.50–8.50	n spectroscopy	^{54}Fe	10469
Fedorov *et al.* [16]	1974	2.90	n spectroscopy	92.90% ^{54}Fe	40286
Almén-Ramström *et al.* [17]	1975	2.50–4.50	n spectroscopy	^{nat}Fe	20788
Mittler *et al.* [18]	1975	1.40–4.00	γ spectroscopy	^{nat}Fe	10519
Korzh *et al.* [19]	1975	2.00–3.00	n spectroscopy	89.51% ^{54}Fe	40531
Guenther *et al.* [20]	1986	1.40–3.60	γ spectroscopy	97.23% ^{54}Fe	13104
Korzh *et al.* [21]	1987	5.00–7.00	n spectroscopy	89.51% ^{54}Fe	32230
Hicks *et al.* [22]	2015	2.00–5.00	γ spectroscopy	97.20% ^{54}Fe	14451

and total inelastic cross sections produced for neutron inelastic scattering measurements on ^{54}Fe. The number of experiments is relatively high, but the covered incident energy range and the number of experimental points is low. Table 1 displays a summary of previous neutron inelastic cross section measurements on ^{54}Fe that reported angle-integrated data. The present measurement is the first one to provide cross sections in the extended energy range starting from the inelastic threshold up to 18 MeV.

Section 2 of the article presents the experimental setup and the consistency checks performed in order to confirm the reliability of the reported data. Section 3 describes the calculations carried out using the TALYS 1.9 code: both with the default input parameters and with the tuned spherical optical model parameters. Our results are discussed in sect. 4 in comparison with theoretical calculations and previous reported results. The sources of uncertainty are detailed in sect. 4.5. Section 5 is dedicated to a brief interpretation of the optical model parameters tuning. Conclusions are given in the last section.

2 Experimental particularities

The experimental setup used for the measurement was previously described in several articles [5,6,23,24]. It consists of the GELINA (Geel Electron Linear Accelerator) neutron source [25] coupled with the GAINS (Gamma Array for Inelastic Neutron Scattering) spectrometer [26] and a fission chamber [27] for normalization.

GELINA is a linear electron accelerator operated by the European Commission, Joint Research Centre (JRC) in Geel, Belgium. The accelerated electrons hit a depleted uranium target producing strong bremsstrahlung. The neutrons are then emitted isotropically following the ^{238}U(γ, n) and ^{238}U(γ, f) reactions. They travel through several flight paths, distributed at various angles and with lengths in the 10–400 m range, up to the measurement cabins where they interact with the samples. The present data were measured on the flight path 3, at a distance of 9967.55 cm from the neutron source, with the GAINS spectrometer by detecting the γ rays generated by the neutron inelastic scattering reactions on the ^{54}Fe nuclei.

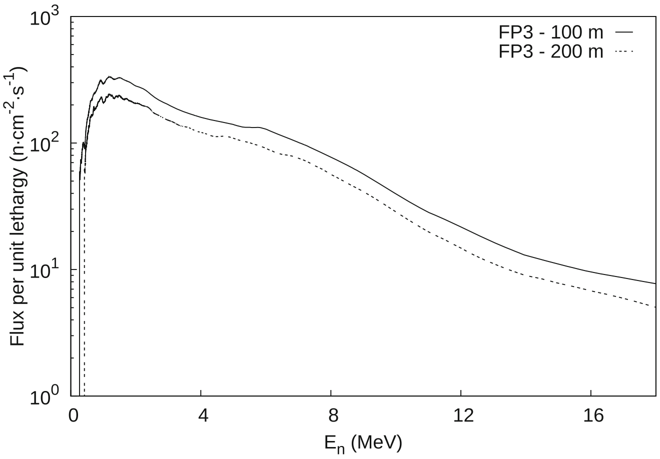

Fig. 1. Comparison between the neutron fluxes (per unit lethargy) in the cabins located on FP3 at a distance of 100 m and 200 m.

The GAINS spectrometer consists of 12 high-purity germanium (HPGe) detectors, placed at 3 different angles (110°, 125°, 150°), with 4 detectors at each angle and at a distance of ≈ 17 cm from the sample. The detection angles were chosen so that the integration procedure of the differential cross sections be as precise as possible (cos(110°) and cos(150°) are the nodes of the 4th degree Legendre

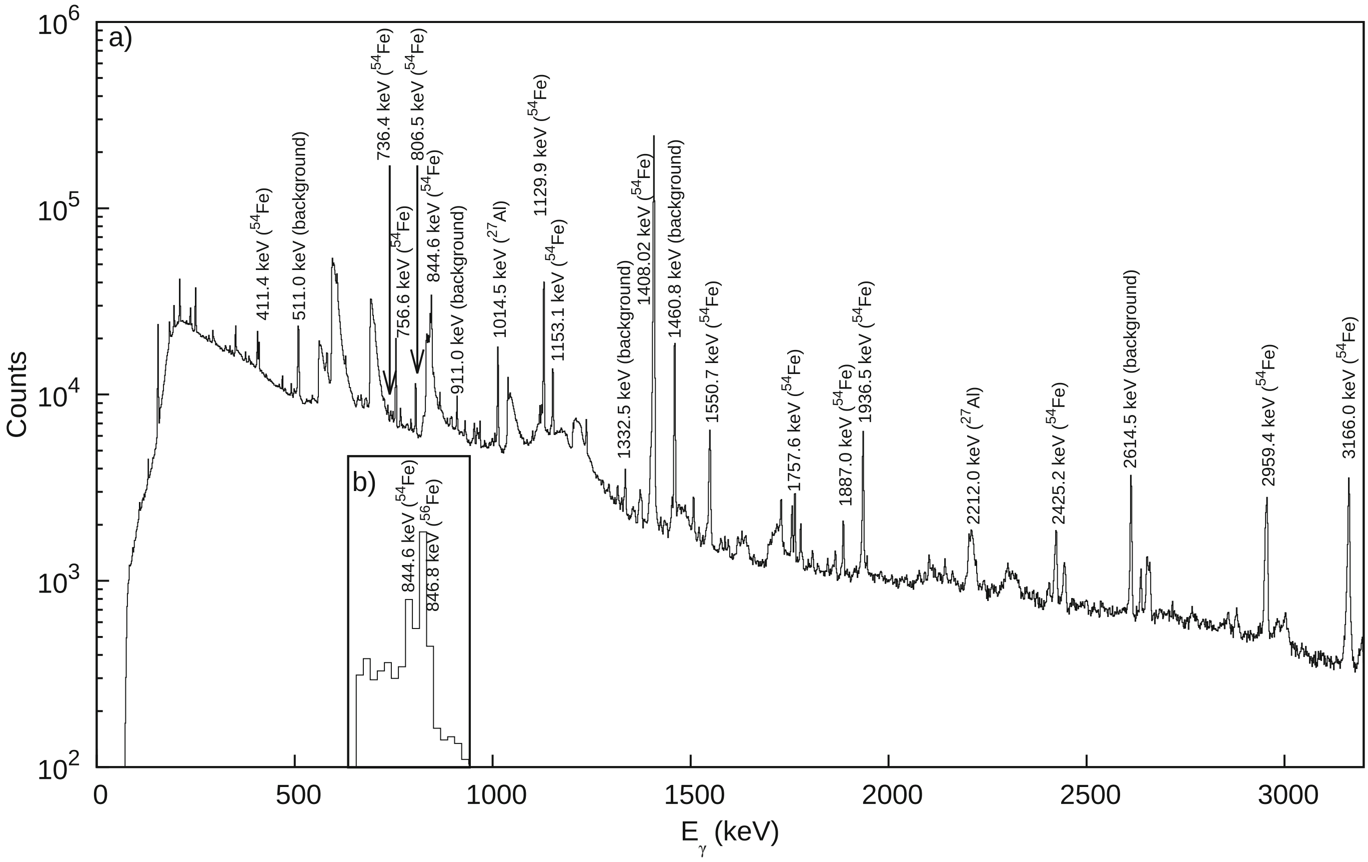

Fig. 2. (a) A γ-ray energy spectrum recorded with one of the HPGe detectors of GAINS. The most intense transitions are indicated and identified. (b) A zoom around the partially overlapping γ rays of 844.6 keV (^{54}Fe) and 846.8 keV (^{56}Fe).

polynomials). The angle-integrated cross sections were obtained using the Gaussian quadrature method [28] coupled with a Legendre polynomial series expansion of the corresponding differential cross sections. The detectors have a relative efficiency of $\approx$ 100% and an energy resolution around 3 keV for the 1332 keV γ line of ^{60}Co.

The incident neutron flux was monitored using a ^{235}U fission chamber located at 211.15 cm upstream the sample. In the measurement cabin the energy-integrated value of the neutron flux was $\approx$ 770 neutrons/(cm^2·s) and the beam was collimated to a diameter of 61.00(50) mm. An important difference between the current measurements and previous ones ([5,6,23,24,29], etc. ...) using GAINS is the length of the flight path. The setup was moved from 200 m to 100 m from the neutron source in 2015. This decrease in flight path length had an impact on the neutron energy resolution, which is now 3 keV at 1 MeV and 80 keV at 10 MeV (previously: 1 keV at 1 MeV and 35 keV at 10 MeV). On the other hand the neutron flux is increased by almost a factor of three. Figure 1 compares the neutron flux measured at the two distances. As we used a ^{235}U fission chamber to monitor the beam, all the reported cross sections are normalized to the ^{235}U(n, f) standard cross sect. [30].

The data acquisition system was digital for the HPGe detectors and analogue for the fission chamber. The signals from the HPGe detectors were read-out by DC440 Acqiris digitizers running at 420 MHz sampling frequency and with 12 bit amplitude resolution and processed online producing time-amplitude listfiles.

One of the key issues in this experiment was the procurement of the sample. Due to the very high price of such a quantity of enriched ^{54}Fe the sample was leased from the Isotope Office of the Oak Ridge National Laboratory. It contained 97.68(7)% ^{54}Fe, 2.24(6)% ^{56}Fe, 0.04(1)% ^{57}Fe and 0.04(1)% ^{58}Fe and had a diameter of 51.00(51) mm, a mass of 19.494(10) g and a thickness of 1.30(1) mm. The calculated areal density corresponding to a pure ^{54}Fe sample was 0.933(18) g/cm^2. Due to the smaller diameter of the sample relative to that of the beam, the uncertainty in the areal density was increased to 2% (see sect. 4.5).

The data analysis procedure is extensively presented in refs. [23,31–33]. For each observed transition coming from the neutron inelastic reaction, displayed in fig. 2, we determine the differential γ-production cross section (for 110°, 125°, 150°) and then we compute the angle-integrated γ-production cross sections. The latter are further used to calculate the level cross sections and the total inelastic cross section. As they are determined using the production cross sections of the observed γ rays, the level cross section and the total inelastic cross section are limited by the number of detected γ rays. The limit up to which

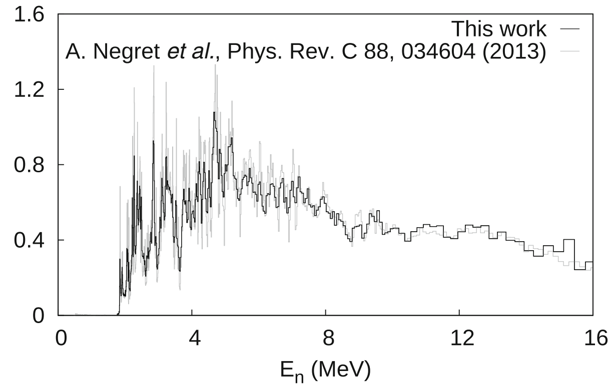

Fig. 3. Comparison between our values for the γ-production cross section of the first transition in ^{28}Si and the ones reported in ref. [34].

they are precise is given by the threshold energy of the first level that decays to the level of interest through a γ ray undetected by us.

To confirm the reliability of our results a consistency check was performed by irradiating a natural sample of silicon for 52 hours. We determined the angle-integrated γ-production cross section for the first transition in ^{28}Si ($E_\gamma = 1778.9\,\mathrm{keV}$). This was compared with previous results from ref. [34] obtained by performing the experiment at the same facility using a similar setup and data analysis procedure but a 200 m flight path. The good agreement displayed in fig. 3 confirms the confidence in our data analysis procedure and experimental setup.

3 Theoretical calculations performed using the TALYS 1.9 code

The experimental results are compared with theoretical calculations performed using the TALYS 1.9 code. The code employs the conventional neutron optical model potential [35]

$$\begin{aligned} U(r,E) = &-V_V(E)f(r,R_V,a_V) - iW_V(E)f(r,R_V,a_V) \\ &+i4a_DW_D(E)\frac{\mathrm{d}}{\mathrm{d}r}f(r,R_D,a_D) \\ &+V_{SO}(E)\left(\frac{\hbar}{m_\pi c}\right)^2\frac{1}{r}\frac{\mathrm{d}}{\mathrm{d}r}f(r,R_{SO},a_{SO})\hat{l}\cdot\hat{\sigma} \\ &+iW_{SO}(E)\left(\frac{\hbar}{m_\pi c}\right)^2\frac{1}{r}\frac{\mathrm{d}}{\mathrm{d}r}f(r,R_{SO},a_{SO})\hat{l}\cdot\hat{\sigma}, \end{aligned} \quad (1)$$

where the function f is the phenomenological Woods-Saxon potential with radius R and diffuseness a while V_V and W_V are the potential depths. In subscript, V, D and SO refer to the volume, the surface and the spin-orbit SO terms, respectively. The proton optical model potential has a similar form but includes an additional Coulomb term.

Two calculations are discussed: one using the default input parameters (labeled TALYS *default*) and another using modified input parameters (labeled TALYS *tuned*). The changes of the default parameters were motivated by the relatively large discrepancy observed between the experimental and the default theoretical shapes of the cross sections plotted in figs. 6, 7, 8 and 9. The goal was to achieve a better theoretical description of the experimental γ-production cross section for the main transition while keeping the other relevant opened reaction channels in agreement with the available experimental data. In this way we ensure that the available reaction strength is appropriately distributed among all open reaction channels. The (n, p) reaction channel ($Q = +0.085\,\mathrm{MeV}$) starts to be significant around 2 MeV and has maximum cross section values around 500 mb for incident energies in the 4–11 MeV range [36–39]. The (n, α) channel ($Q = +0.844\,\mathrm{MeV}$) is relevant starting around 5 MeV and has a maximum cross section below 100 mb [39–41].

The TALYS *default* calculation is straightforward and can be performed using an input file with only a few simple keywords. The default optical model potentials are using the local and global parameterizations of Koning and Delaroche [42]. The γ-ray strength functions, important for the characterization of the γ-emission channel, are described using the generalized Lorentzian form of Kopecky and Uhl [43,44] for the $E1$ transitions and the Brink-Axel option [45,46] for the others. The level density is calculated using the Gilbert and Cameron approach [47] via the constant temperature model for low excitation energies and the backshifted Fermi gas model, with an energy dependent parameter accounting for the damped shell effects proposed by Ignatyuk *et al.* [48], for higher excitation energies. The discrete level scheme is taken from the Reference Input Parameter Library (RIPL-3) data base [49] and extended using theoretical level densities. In situations with unknown spins, parities and branching ratios TALYS always assigns values based on statistical spin rules.

The TALYS *tuned* calculation was performed starting from the default calculation. The best agreement between the experimental results and the theoretical predictions was obtained by modifying three parameters of the spherical optical model. First, the radius (R_V) associated with the *proton* volume-central terms was increased by 1.5%. Further, the diffuseness (a_D) of the *neutron* surface-central component was decreased by 27% while the radius (R_D) of the same component was increased by 7%. The level density was calculated using a more microscopic approach based on the Hartree-Fock-BCS method and employing the Skyrme force (MSk7) coupled with a δ-function pairing force and a phenomenological Wigner term [50]. These changes had a big impact at low and intermediary incident energy ranges except for the level densities which impacted the intermediate and the high energy regions of the inelastic cross sections. In particular, the diffuseness and to a somewhat lesser extent the radius parameter of the neutron surface-derivative term show considerable impact above 2.5 MeV for the 1408.1 keV transition (see fig. 5).

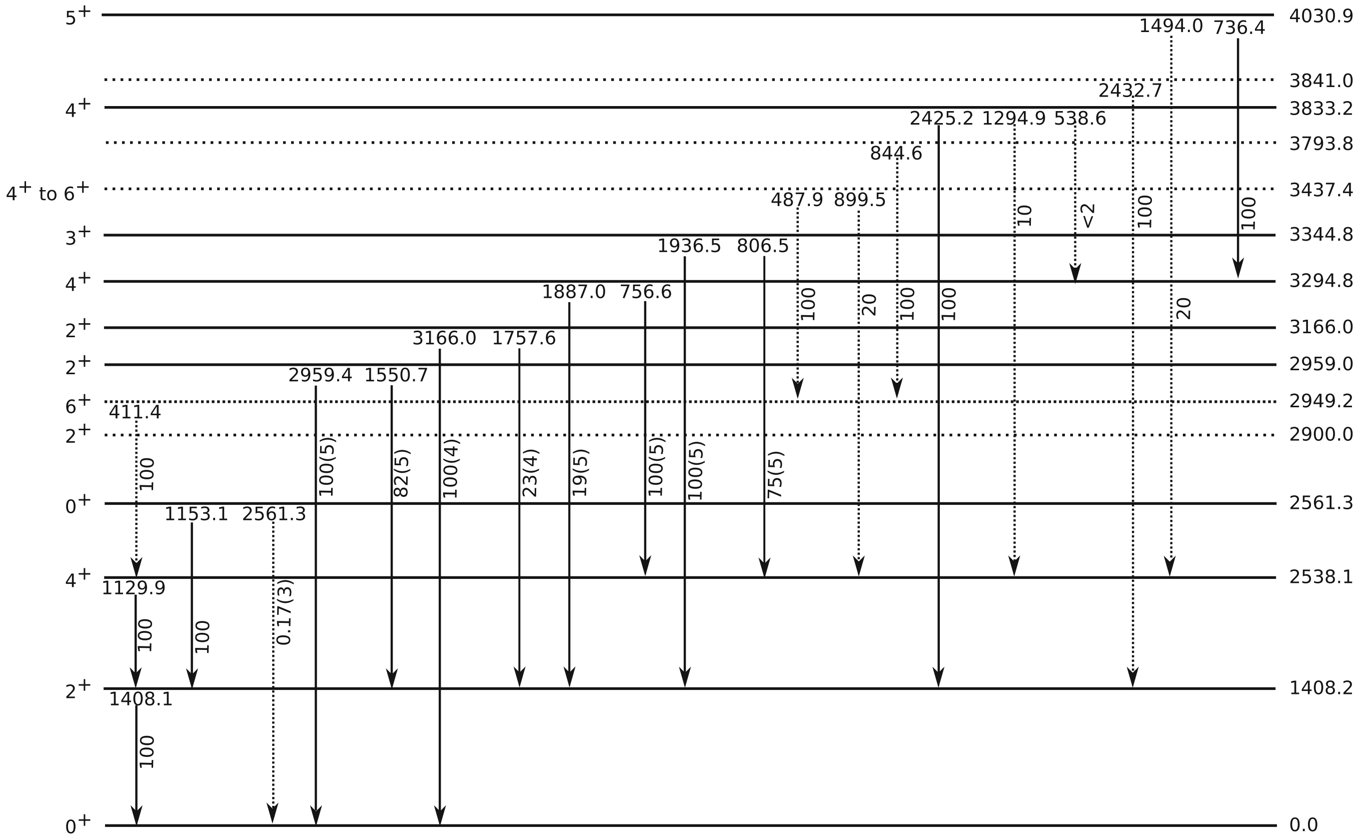

Fig. 4. A reduced level scheme of ^{54}Fe adapted from ref. [51]. The observed transitions are displayed with solid arrows while for the unobserved ones we used dashed lines.

4 Results and discussion

Figure 4 displays a partial level scheme of ^{54}Fe taken from ref. [51]. We identified 13 transitions corresponding to the neutron inelastic scattering on ^{54}Fe (indicated by solid arrows in fig. 4). The five levels displayed with dashed lines (2900.0, 2949.2, 3437.4, 3793.8 and 3841.0 keV) do not have associated γ rays detected in the present measurement with the exception of the 2949.2 keV level for which the 411.4 keV transition was observed but was difficult to integrate because it was partially overlapping with the 407.5 keV γ ray coming from the (n, p) reaction. Therefore, the production cross section of this transition is not reported. The 2900.0 keV level was observed only in a ^{54}Fe(e, e$'$) experiment [52,53] and has no known de-exciting transitions. We analysed our amplitude spectra searching for all the decay possibilities of such an excited level and no suitable peaks were observed. Further, this level is also not included in the default level scheme used by TALYS 1.9. According to our results, the existence of this level is questionable or it decays through γ transitions with cross section values below our sensitivity limit (around 10 mb). The 3437.4 keV level decays through two γ rays (487.9 and 899.5 keV), none of them being observed in the present work. It was only observed in a ^{54}Fe(^{3}He, γn2p) experiment [54] together with the 3793.8 keV level. The 844.6 keV γ ray de-excites this latter level and it was observed in our experiment but the corresponding peak could not be integrated because it was on top of a "neutron triangle" (coming from the inelastic scattering of neutrons on the germanium nuclei) and very close to the main transitions in ^{56}Fe ($E_\gamma = 846.8$ keV) and ^{27}Al ($E_\gamma = 843.6$ keV) (see fig. 2 (b)). The last excited level plotted with a dashed line in fig. 4 has no assigned spin and parity and decays through a 2432.7 keV γ ray, which remained unobserved.

For each detected γ ray we determined the corresponding production cross section. Using these values we calculated the first excited level and the total inelastic cross sections. When two or more γ rays from the same level were observed we used the corresponding γ-production cross sections to calculate the branching ratios of the transitions.

4.1 γ-production cross sections

Figures 6 and 7 display the comparison between our experimental results for the production cross sections of the observed transitions, previous experimental values and theoretical calculations performed with the TALYS 1.9 code. While the agreement between the experimental results is mostly good, the one with the TALYS *default* theoretical calculations leaves much to be desired. The values

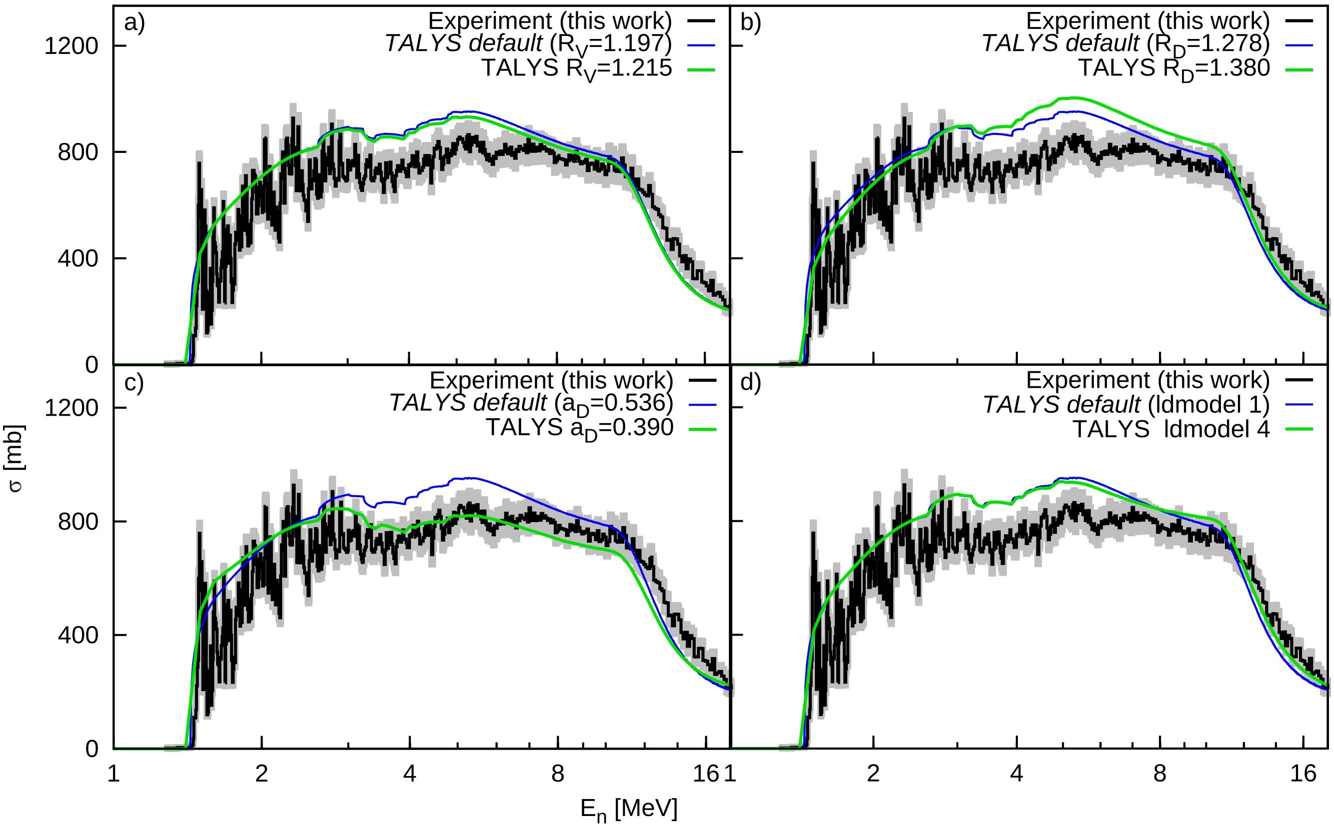

Fig. 5. (Color online) The γ-production cross section of the main transition $E_\gamma = 1408.1\,\text{keV}$. The impact of each optical model parameter (R_V, R_D, a_D, level density model) modification is shown separately as compared with the default calculation and the experimental results.

predicted by TALYS *default* calculations are comparable with the experimental points but the shapes of the cross sections are different. The comparison of the experimental results with the TALYS *tuned* predictions reveals a much better agreement for the first transition and improvements for the remaining transitions, especially at low neutron energies.

The production cross section of the first transition is presented in fig. 6. Resonant shapes are observed both in our results and in the ones of Guenther *et al.* [20] at energies below 3 MeV. Above 3 MeV, the cross section displays a somewhat smoother behaviour generated by the overlap of many resonances in the compound system. The maximum value is around 800 mb and the cross section stays close to its maximum value over a fairly large neutron-energy range. The total relative uncertainty is under 5% for most of the incident energy range. According to the TALYS 1.9 calculation this transition represents the major contributor to the total inelastic cross section (90% of all inelastic strength).

The production cross sections of the other observed transitions are displayed in fig. 7. When compared with the measurement reported in ref. [20], having incident energies in a limited range (1.4–3.6 MeV) and rather high uncertainties, the agreement is very good. For the 1129.9 keV γ-production cross section we also plotted the data from ref. [22] (where the excitation function is reported in arbitrary units) in order to show the good agreement between the shape of the two cross sections.

The comparison between theory and experiment shows rather poor agreement. In most of the cases TALYS *default* calculation is not able to reproduce neither the shape nor the absolute values of the experimental results. However, when tuning the code parameters, the experimental cross sections near their respective maxima are better described, but above 5 MeV the predictions are substantially below the data. In ref. [6] a similar problem was attributed to the population of compound nucleus states, a point that is not investigated further here since it warrants a more systematic approach [55–57]. The reported maximum cross sections displayed in fig. 7 vary from 300 mb down to 20 mb with total relative uncertainties below 10% for most of the incident energy range. The panels (c)-(d), (e)-(f), (g)-(h) and (i)-(j) of fig. 7 display γ-production cross sections for transitions decaying from the same level. Their values were used to calculate the corresponding branching ratios presented in sect. 4.4.

4.2 Level cross section

The level cross section is the probability of leaving the nucleus in a given excited state following the neutron scat-

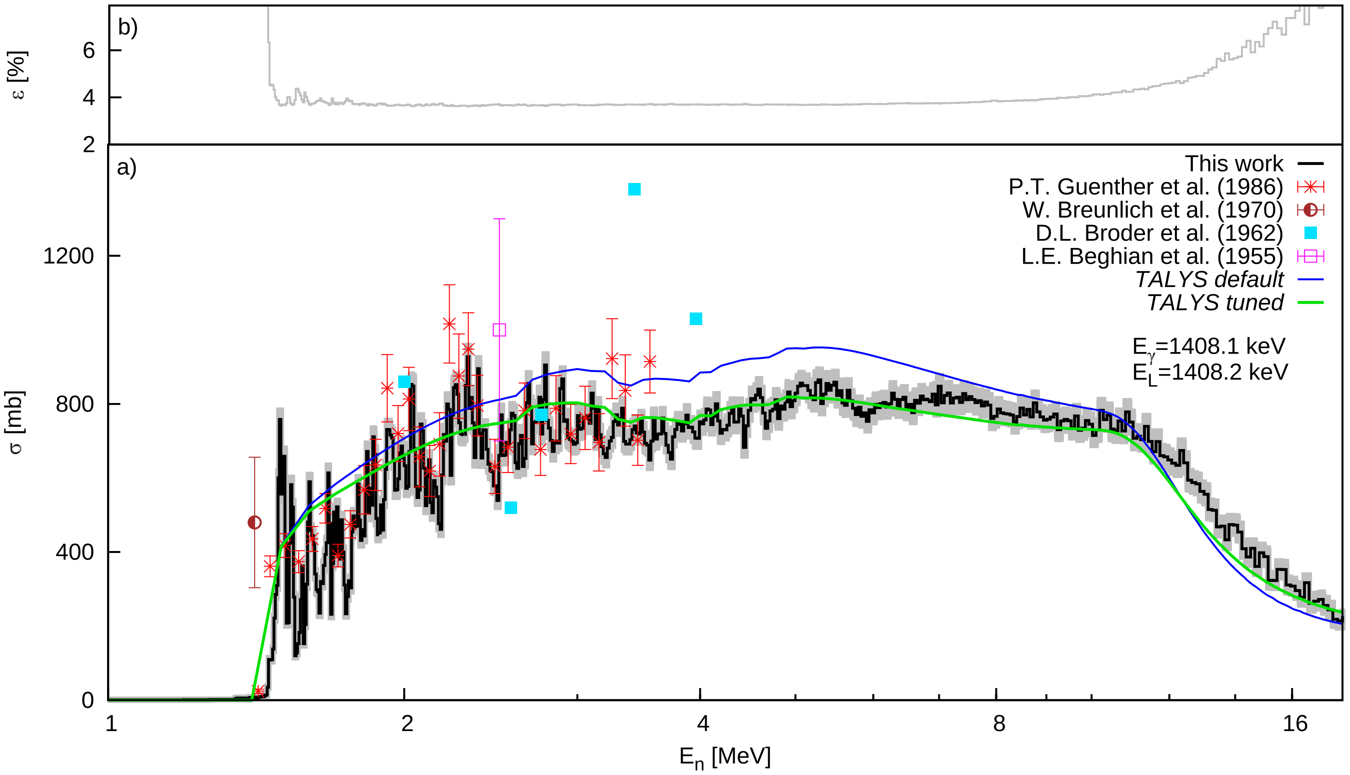

Fig. 6. (Color online) (a) The γ-production cross section of the most intense transition in ^{54}Fe and (b) the corresponding total relative uncertainty. The present experimental results are compared with previous values and TALYS 1.9 theoretical calculations.

tering, with the feeding from higher levels subtracted. It was calculated for the first excited state in ^{54}Fe and is compared in fig. 8 with previously reported results and with TALYS calculations. Our values are precise up to an incident energy from where we do not subtract anymore the feeding because we did not detect the corresponding transitions. Above those energies our results are only higher limits of the level cross sections (see fig. 8 where outside the precision range the experimental results remain constant while the theoretical calculations continue to decrease). The energy limits and the formula used to calculate the level cross section are displayed in table 2 and are based on nuclear structure information taken from ref. [51]. The agreement between most of the experimental results is fairly good. The exception is the data reported by Mittler *et al.* [18] for the 1408.2 keV level which has higher values at incident energies above 2.5 MeV. The authors used also γ spectroscopy but on a natural target (with only 5.85(11)% ^{54}Fe abundance) so it might be that the achieved statistics for the transitions feeding the level was rather limited (see the formula from table 2). When comparing the experimental results with the theoretical predictions we note, also for this case, that TALYS *tuned* calculation gives better results. This improvement in the level cross section is the best indicator that the changes we made to the neutron optical potential are suitable. The level cross section has maximum values around 800 mb and total relative uncertainties less than 10% in the precision range.

4.3 Total inelastic cross section

The total neutron inelastic cross section is calculated as a sum of the production cross sections of all transitions that feed the ground state. The threshold energy of the first unobserved transition that feeds the ground state gives the precision limit. Above this incident energy, our experimental results are only lower limits of the total inelastic cross section. The formula used to calculate the total inelastic cross section is displayed on the first row of table 2 together with the precision limit. One should note that the limit is given by the threshold energy of the 4578.5 keV excited level which decays to the ground state through the 4579.0 keV γ ray undetected by us. This is the case despite the fact that there are two intermediate levels (2561.3 keV and 4290.8 keV) which decay to the ground state through $E0$ transitions, hence impossible to detect using HPGe detectors. However, we were able to take into account the 2561.3 keV transition using the observed 1153.1 keV γ ray (decaying from the same level) and the known 0.17(3)% branching ratio [58] measured by observing the $e^+ - e^-$ internal pairs emitted by the 2561.3 keV, 0^+ level [58]. The second $E0$ transition was neglected when calculating the total inelastic cross section and the precision limit mentioned above. This was done because it has no known branching ratio and it is reasonable to assume that its contribution is very small, among others, due to the relatively high energy.

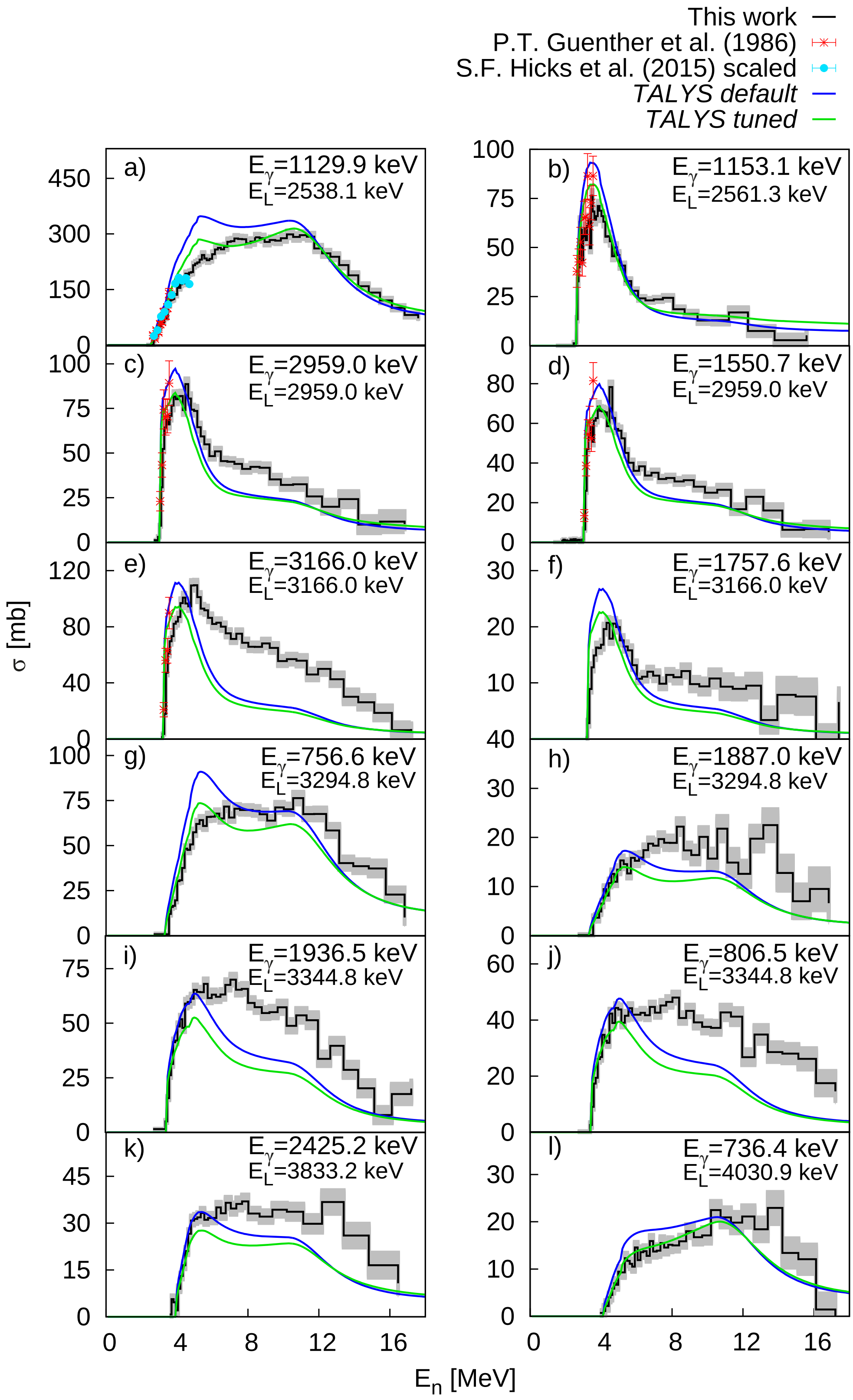

Fig. 7. (Color online) The γ-production cross sections of other transitions in ^{54}Fe observed in the present experiment. The gray bands correspond to the total uncertainties.

Table 2. The formulas used to calculate the total inelastic cross section and the 1408.2 keV level cross section and the incident energies up to which our results are precise.

E_L [keV]	Formula	Limit [keV]
0 (g.s.)	$\sigma_{1408.1}(E_n) + 0.17\sigma_{1153.1}(E_n) + \sigma_{2959.4}(E_n) + \sigma_{3166.0}(E_n)$	4664.1
1408.2	$\sigma_{1408.1}(E_n) - \sigma_{1129.9}(E_n) - \sigma_{1153.1}(E_n) - \sigma_{1550.7}(E_n) - \sigma_{1757.6}(E_n) - \sigma_{1887.0}(E_n) - $ $-\sigma_{1936.5}(E_n) - \sigma_{2425.2}(E_n)$	3912.8

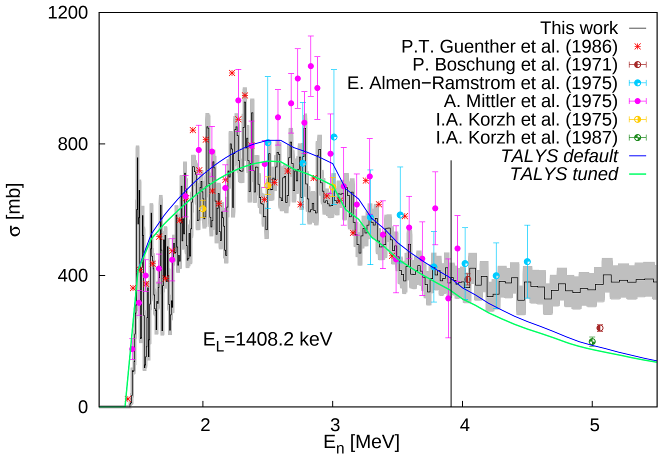

Fig. 8. (Color online) The cross section of the first excited level in ^{54}Fe. The gray band corresponds to the total uncertainties and the black vertical line displays the upper limit of our precision range.

Comparing our total inelastic cross section with previous measurements we note a generally good agreement (see fig. 9). TALYS *default* predicts higher values up to around 12 MeV and lower above this incident energy. TALYS *tuned* is, as expected, in very good agreement with the experimental results. The comparison between the experimental results and the evaluated libraries ENDF/B-VIII.b5 [59] and TENDL-2017 [60] shows higher evaluated values up to around 11 MeV and smaller above. The evaluated data from CENDL-3.1 [61] library has a different shape and lie below the experimental results up to ≈ 10 MeV. The other evaluated libraries such as JENDL-4.0 [62], JEFF-3.2 [63] and ROSFOND-2010 [64] are not displayed in fig. 9 because they are very similar to the ones already shown.

The total inelastic cross section has a maximum value of 1.05(5) b at an incident energy of 5.3 MeV. The total relative uncertainties are below 5% up to 10 MeV and increase up to around 10% at 18 MeV.

The resonant region observed at low energies in the total inelastic cross section was investigated (as in refs. [5, 23]) in order to understand if the observed structures represent individual levels in the ^{55}Fe compound nucleus or only the overlapping of such states. Reference [5] presented the same study for ^{56}Fe and concluded that in the first few hundreds keV the observed resonances correspond, at least partially, to individual states in the ^{57}Fe compound nucleus. In the present study, the number of observed structures is much smaller than the theoretical level density in ^{55}Fe. We conclude that, even at very low incident energies, the individual resonances could not be resolved. This difference is partially due to a higher neutron separation energy ($S_n = 9.3$ MeV) in ^{55}Fe than in ^{57}Fe ($S_n = 7.6$ MeV), which translates to higher energy states being populated in ^{55}Fe, and therefore to a higher level density.

4.4 Branching ratios

In four cases two γ rays decaying from the same level were detected. For these transitions we calculated the branching ratios as a ratio of the γ-production cross sections of the two transitions, for each incident energy. The resulting values were further averaged (excluding the discrepant values) and are compared in table 3 with values taken from ref. [51]. The agreement is reasonable and our uncertainties are smaller. This gives us additional confidence in the measured γ-production cross sections while the reported branching ratios are of importance for the nuclear structure evaluations of the ^{54}Fe nucleus.

4.5 Uncertainties

Given the high precision we claim, a short discussion on uncertainties is in order considering that these values represent a quantitative indication of the data quality. Two types of uncertainties can be identified: one arising from statistics and one coming from the measurement tools. The first one is kept as low as possible by increasing the measurement time or by rebinning the time-of-flight channels when needed. Usually, this procedure is performed at neutron energies where the cross section is structureless.

In the present measurement the uncertainty per channel coming from the γ-ray yields of each detector, for the strongest transition, is below 4% up to 8 MeV and stays smaller than 20% for higher incident energies. In the same energy range this corresponds to less than 1.6% and than 7.6%, respectively, in the integrated cross section when adding the statistics from all detectors.

For the fission chamber yield we have an associated uncertainty of 2% from statistics which was further decreased by a smoothing technique performed with a double-smooth procedure, each smooth consisting of a 61 channels second-order polynomial fit.

Other sources of uncertainty are displayed in table 4.

As compared to all other previous measurements performed by our group, a special issue in the present experiment was the fact that the ^{54}Fe sample was smaller

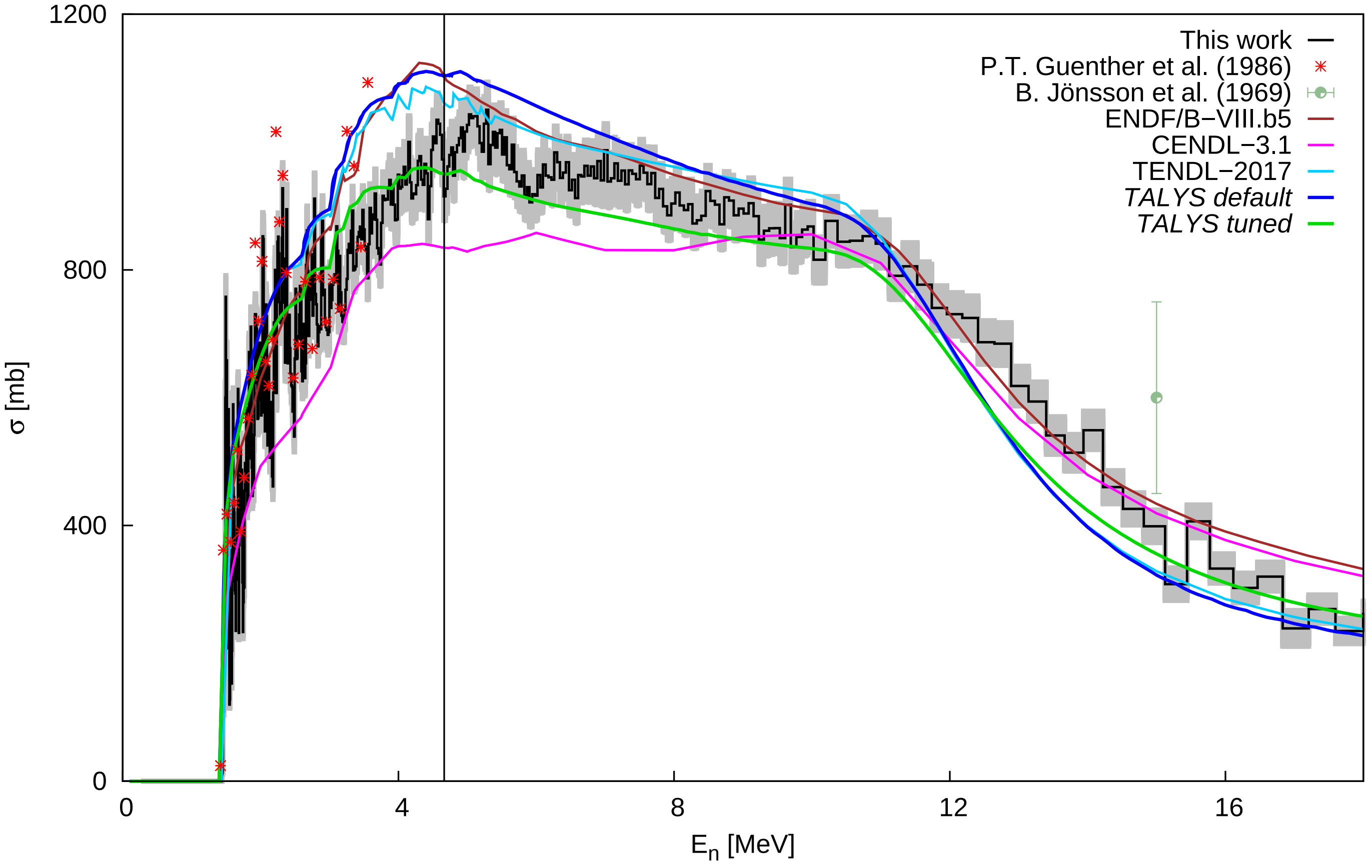

Fig. 9. (Color online) The total neutron inelastic cross section of ^{54}Fe. The gray band represents the total uncertainties and the black vertical line marks the upper limit of our precision range.

Table 3. The comparison between the branching ratios of several transitions in ^{54}Fe, calculated using the corresponding γ-production cross sections, and literature values taken from ref. [51].

E_L [keV]	E_γ [keV]	Branching ratio [%] this work	ref. [51]
2959.0	2959.4	100	100(5)
	1550.7	77(2)	82(5)
3166.0	3166.0	100	100(4)
	1757.6	18(1)	23(4)
3294.8	756.6	100	100(5)
	1887.0	26(3)	19(5)
3344.8	1936.5	100	100(5)
	806.5	68(1)	75(5)

Table 4. Sources of uncertainty and their associated relative values in the present experiment.

Source	Uncertainty [%]
efficiency of the HPGe detectors	≈ 2–4
efficiency of the fission chamber	≈ 2
fission cross section of ^{235}U	< 1
areal density of the sample	≈ 2
thickness of the FC deposits	< 1
multiple scattering correction factor	< 1

than the neutron beam. The neutron beam diameter was 61.0(5) mm, with the uncertainty determined from the analysis of the beam profile observed with a neutron camera, and it is significantly smaller than the diameter of the fission chamber deposits. The sample diameter was 51.0(5) mm. This difference in beam-sample dimension was taken into account when analyzing the data. To account for any potential irregularities in the shape of the sample we increased its areal density uncertainty to 2%.

The uncertainties of the detector efficiencies are coming mainly from the activity and the position of the calibration source.

Our reported total relative uncertainty for the production cross section of the first transition is below 5% up to 10 MeV and less than 8% up to 18 MeV (see fig. 6). For the other γ-production cross sections the uncertainties are around 10% for most of the incident energy range.

Table 5. Values of the three optical model parameters modified in the present work in order to improve the agreement with the measured cross sections. The usual range of values compiled in ref. [65] is also shown for comparison.

Parameter	TALYS *default*	TALYS *tuned*	Parameter range as in ref. [65]
R_V	1.197	1.215	1.090–1.322
a_D	0.536	0.390	0.255–1.000
R_D	1.278	1.380	1.050–1.300

5 Interpretation of the theoretical calculations

Considering the significantly improved agreement between the theoretical calculation and the experimental data achieved through the parameters tuning described in sect. 3, we will dedicate this section to a (partial) interpretation of the optical model parameter modifications. We emphasize that during the modifications all the parameters were kept within physical limits [65] (see table 5). Figure 5 shows how the change of each parameter impacted the γ-production cross section of the first transition in ^{54}Fe.

The parameter tuning procedure started by trying to improve the theoretical prediction for the $^{54}\mathrm{Fe(n,p)}^{54}\mathrm{Mn}$ channel which is a well known dosimeter reaction with evaluated data available in the IRDFF (International Reactor Dosimetry and Fusion File) data base [66,67] (see fig. 10(c)). As expected, by increasing the R_V for protons by 1.5% the $(\mathrm{n,p})$ reaction cross section increased in the incident energy range from the $(\mathrm{n,p})$ reaction threshold up to around 13 MeV. At the same time the $(\mathrm{n,n'})$ and the (n,α) reaction cross sections decreased keeping the total cross section constant.

The decrease of the diffuseness a_D of the surface-central neutron optical model potential by 27% resulted in a decrease of all the relevant non-elastic cross sections, while the elastic one increased in the intermediary incident energy range. This behaviour is not surprising considering that this modification lowered the contribution of the surface-central term to the total potential, hence, generating a decrease of the absorbed incident flux. At the same time, a smaller diffuseness value can be interpreted as making the target nucleus more rigid against the incident flux. This increased rigidity generates a larger contribution of the shape elastic (reflexion) part of the optical model potential which results in higher values of the elastic cross section (as observed in fig. 10(b)). The small decrease of the elastic cross section below $E_n = 3\,\mathrm{MeV}$ can be explained by the smaller absorbed incident flux and by taking under consideration that the compound elastic component is significant in this incident energy range.

An interesting behaviour was observed when increasing the radius R_D of the surface-central component of the neutron optical model potential by 7%. This decreased

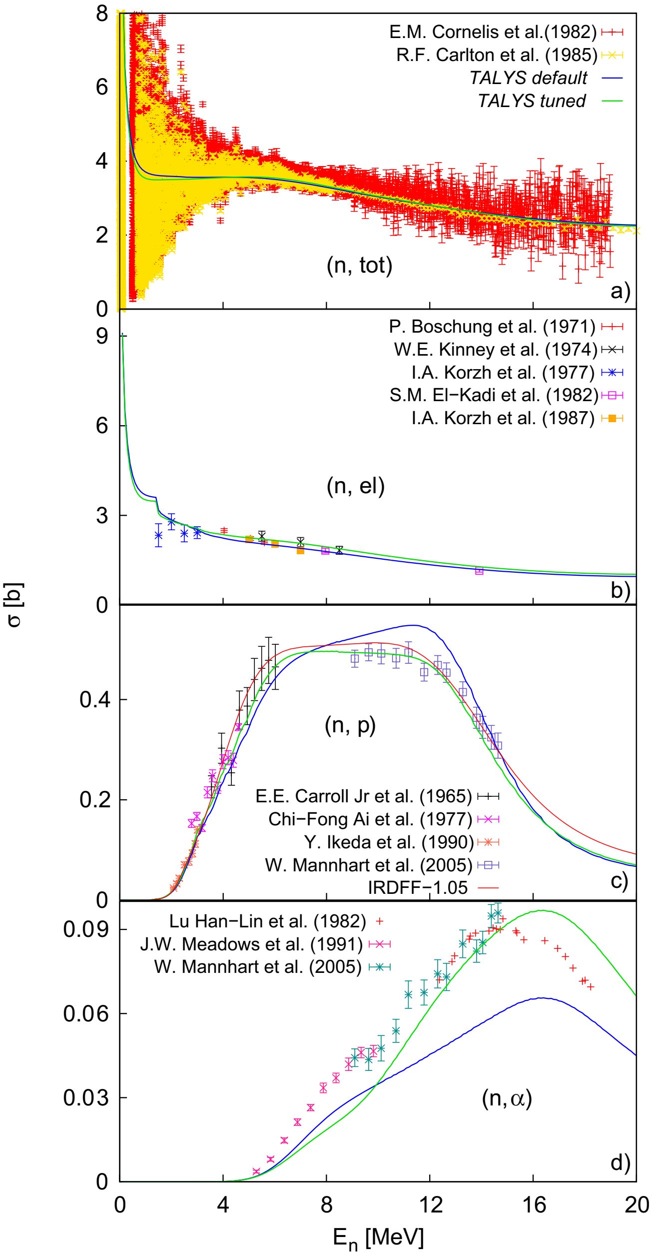

Fig. 10. (Color online) Relevant reaction channels open when incident neutrons with $E_n < 20\,\mathrm{MeV}$ interact with a ^{54}Fe target nucleus.

the inelastic cross section for low incident energies (up to 3 MeV) and increased it for higher energies. All the other relevant cross sections were increased by this modification.

From figs. 6 and 7(a), (b), one can see that the parameter changes generated considerable improvements in describing the experimental data in the entire incident energy range. However, this is not the case for the transitions decaying from excited levels with energies higher than 2959.0 keV (see fig. 7(c)–(l)), where only the small incident energy region (peak height) is improved but not the tail. This severe underestimation indicates missing feeding from higher-lying levels. Even though the TALYS *tuned* calculation greatly improved the agreement for the most intense transitions, the changes between tuned and default are too small to explain the remaining difference and, therefore, optical model potential and/or level densities are not the main cause of these discrepancies. This might be caused by the fact that TALYS wrongly predicts the initial population and decay of the compound nucleus levels. As mentioned, this was also the case in our previous study which reported neutron inelastic cross sections on ^{57}Fe [6]. Finally, nuclear structure could also be a reason for example if decays along collective bands by $E2$ transitions are preferred rather than statistical $E1$ transitions only.

Figure 10 shows that the present tuning of the optical model parameters was done under the constraint of keeping the total, the elastic and the most relevant reaction cross sections ((n,p) and (n,α)) within the limits given by the experimental results [36–41, 68–74]. Indeed, the TALYS *tuned* values describe much better (as compared to TALYS *default*) the available experimental results for the (n,p) and (n,α) reaction channels.

The authors of ref. [75] measured the emitted neutrons following the neutron elastic and inelastic scattering on ^{54}Fe and determined their angular distributions for the 2–6 MeV incident energy range. Even though they show that the TALYS default calculation gives good results in reproducing the experimental values (especially the elastic cross section), some discrepancies associated to the inelastic channel were observed at higher energies. In consequence, the authors performed modifications of the TALYS default parameters in order to improve the agreement with the experimental data. Reference [75] states that when adjusting optical potential parameters (such as R_V, R_D, a_D ...) a good description of the inelastic cross sections was not possible without harming the elastic one. Consequently, they chose to modify the DWBA deformation parameter β_2. A substantial modification (25–50%) of β_2 was needed to properly describe the inelastic channel above 5 MeV incident energy.

Our data, as the angular distributions from ref. [75], display a larger disagreement relative to the TALYS *default* calculations above $E_n = 5\,\mathrm{MeV}$. Both our TALYS *tuned* calculation and the one presented in ref. [75] required an increase of the surface absorption region in order to improve the agreement in this energy range. We implemented this by directly increasing the radius of the surface-central term of the neutron optical model potential, while Vanhoy *et al.* [75] raised the deformation parameter. This is supported to some extent by the arguments given in ref. [75] (and references therein) where it is stated that ^{54}Fe displays a relatively strong collective behaviour so that a coupled channels calculation may be needed instead of a simple spherical optical model potential in order to better describe the larger deformation induced by higher energy incident neutrons.

Also, nucleon scattering in the iron region was previously described using a dispersive coupled-channels optical-model (DCCOM) [76], [77] or with l-dependent optical model parametrisations [78]. The DCCOM approach does not seem to describe well the neutron total cross section of ^{nat}Fe bellow 4 MeV [79]. Figure 10 shows that the ^{54}Fe total cross section is in better agreement with our TALYS calculation (which does not employ coupled-channels) although this prediction seems to be similar to the DCCOM results for ^{nat}Fe.

6 Conclusions

The present experiment measured the production cross sections of thirteen γ rays emitted in the $^{54}\mathrm{Fe}(\mathrm{n},\mathrm{n}'\gamma)^{54}\mathrm{Fe}$ reaction. Our experimental results were compared with previous reported values and with theoretical calculations performed with the TALYS 1.9 code. The level cross sections and the total inelastic cross section were determined using the γ-production cross sections. Up to 10 MeV incident neutron energy, the total relative uncertainty for the strongest transition is less than 5% and increases up to 8% at 18 MeV. The other reported γ-production cross sections have total relative uncertainties less than 10% for most of the incident energy range. For the cases where more than one transition was decaying from a given level we calculated the corresponding branching ratios and the experimental results were compared with evaluated values.

The relatively poor agreement between our experimental data and the values predicted by a default TALYS calculation motivated the dedicated calculation labeled TALYS *tuned*. A significantly improved agreement between the theoretical and the experimental cross sections is obtained by increasing the radius associated to the *proton* volume-central term and by increasing the radius and decreasing the diffuseness of the *neutron* surface-central component term. The use of a more microscopic approach when calculating the level density also improved this agreement. The parameter modification we employed in order to better describe the experimental data (both our inelastic and other channels) has the significance of an increase of the surface absorption region and the rigidity of the ^{54}Fe nucleus when interacting with neutrons.

This is the first experimental data set on ^{54}Fe that covers an extended energy range (from the inelastic threshold and up to 18 MeV) while having such small uncertainty values.

This work was supported by the European Commission within the Seventh Framework Programme through Fission-2013-CHANDA (project no. 605203) and EUFRAT (project no. 211499), and by the Ministry of Research and Innovation of Romania, CNCS-UEFISCDI, through project no. PN-III-P4-ID-PCE-2016-0025 within PNCDI III. The authors would like to thank the Institut de Radioprotection et de Sûreté Nucléaire (IRSN) for providing financial support for sample acquisition under the agreement JRC-3465 and IRSN-LS20361. We further like to thank Arjan Koning for his prompt suggestion for the final TALYS calculation, the support team of GELINA for providing the conditions of the experiment and the staff of the Radionuclide metrology sector of JRC Geel for monitoring the evolution of activity in the sample. The enriched sample used in this research was supplied by the United States Department of Energy Office of Science by the Isotope Program in the Office of Nuclear Physics.

References

1. J. Meija, T.B. Coplen, M. Berglung, W.A. Brand, P. De Bièvre, M. Gróning, N.E. Holden, J. Irrgeher, R.D. Loss, T. Walczyk, T. Prohaska, Pure Appl. Chem. **88**, 293 (2016).
2. Nuclear Energy Agency, OECD, Collaborative International Evaluated Library Organisation (CIELO) Pilot Project, WPEC Subgroup 40 (SG40) `https://www.oecd-nea.org/science/wpec/sg40-cielo` (Online; accessed 28 November 2017).
3. M.B. Chadwick, R. Capote, A. Trkov, M.W. Herman, D.A. Brown, G.M. Hale, A.C. Kahler, P. Talou, A.J. Plompen, P. Schillebeeckx, M.T. Pigni, L. Leal, Y. Danon, A.D. Carlson, P. Romain, B. Morillon, E. Bauge, F.-J. Hambsch, S. Kopecky, G. Giorginis, T. Kawano, J. Lestone, D. Neudecker, M. Rising, M. Paris, G.P.A. Nobre, R. Arcilla, O. Cabellos, I. Hill, E. Dupont, A.J. Koning, D. Cano-Ott, E. Mendoza, J. Balibrea, C. Paradela, I. Durán, J. Qian, Z. Ge, T. Liu, L. Hanlin, X. Ruan, W. Haicheng, M. Sin, G. Noguere, D. Bernard, R. Jacqmin, O. Bouland, C. De Saint Jean, V.G. Pronyaev, A.V. Ignatyuk, K. Yokoyama, M. Ishikawa, T. Fukahori, N. Iwamoto, O. Iwamoto, S. Kunieda, C.R. Lubitz, M. Salvatores, G. Palmiotti, I. Kodeli, B. Kiedrowski, D. Roubtsov, I. Thompson, S. Quaglioni, H.I. Kim, Y.O. Lee, U. Fischer, S. Simakov, M. Dunn, K. Guber, J.I. Márquez Damián, F. Cantargi, I. Sirakov, N. Otuka, A. Daskalakis, B.J. McDermott, S.C. van der Marck, Nucl. Data Sheets **148**, 189 (2018).
4. M. Herman, A. Trkov, R. Capote, G.P.A. Nobre, D.A. Brown, R. Arcilla, Y. Danon, A. Plompen, S.F. Mughabghab, Q. Jing, G. Zhigang, L. Tingjin, L. Hanlin, R. Xichao, L. Leal, B.V. Carlson, T. Kawano, M. Sin, S.P. Simakov, K. Guber, Nucl. Data Sheets **148**, 214 (2018).
5. A. Negret, C. Borcea, Ph. Dessagne, M. Kerveno, A. Olacel, A.J.M. Plompen, M. Stanoiu, Phys. Rev. C **90**, 034602 (2014).
6. A. Negret, M. Sin, C. Borcea, R. Capote, Ph. Dessagne, M. Kerveno, N. Nankov, A. Olacel, A.J.M. Plompen, C. Rouki, Phys. Rev. C **96**, 024620 (2017).
7. N. Otuka, E. Dupont, V. Semkova, B. Pritychenko, A.I. Blokhin, M. Aikawa, S. Babykina, M. Bossant, G. Chen, S. Dunaeva, R.A. Forrest, T. Fukahori, N. Furutachi, S. Ganesan, Z. Ge, O.O. Gritzany, M. Herman, S. Hlavač, K. Katō, B. Lalremruata, Y.O. Lee, A. Makinaga, K. Matsumoto, M. Mikhaylyukova, G. Pikulina, V. G. Pronyaev, A. Saxena, O. Schwerer, S.P. Simakov, N. Soppera, R. Suzuki, S. Takács, X. Tao, S. Taova, F. Tárkányi, V.V. Varlamov, J. Wang, S.C. Yang, V. Zerkin, Y. Zhuang, Nucl. Data Sheets **120**, 272 (2014).
8. V.V. Zerkin, B. Pritychenko, Nucl. Instrum. Methods Phys. Res. A **888**, 31 (2018).
9. L.E. Beghian, D. Hicks, B. Milman, Philos. Mag. **46**, 963 (1955).
10. D.L. Broder, A.I. Lashuk, I.P. Sadokhin, A.P. Suvorov, *Theory and Method of Nuclear Reactor Design* (Gosmatomizdat, Moscow, 1962) p. 254.
11. R.W. Benjamin, I.L. Morgan, Phys. Rev. **163**, 1252 (1967).
12. B. Jönsson, K. Nyberg, I. Bergqvist, Ark. Fys. **39**, 295 (1969).
13. W. Breunlich, G. Stengl, H. Vonach, Z. Naturforsch. A **26**, 451 (1971).
14. P. Boschung, J.T. Lindow, E.F. Shrader, Nucl. Phys. A **161**, 593 (1971).
15. W.E. Kinney, F.G. Perey, Oak Ridge National Lab. reports, 4907 (1974).
16. M.B. Fedorov, T.I. Jakovenko, Ukr. Fiz. Zh. **19**, 152 (1974).
17. E. Almén-Ramström, in *Conference on Nuclear Data for Reactors, Helsinki*, Vol. **2** (International Atomic Energy Agency, Vienna, 1970) p. 349.
18. J. Nardini, *Neutron inelastic scattering cross sections for natural iron via* $(\mathrm{n},\mathrm{n}'\gamma)$ *reactions*, Master Thesis (1975).
19. I.A. Korzh, V.A. Mishchenko, E.N. Mozhzhukhin, A.A. Golubova, N.M. Pravdivyj, I.E. Sanzhur, M.V. Pasechnik, Yad. Fiz. Issled. Rep. **25**, 63 (1977).
20. P.T. Guenther, D.L. Smith, A.B. Smith, J.F. Whalen, Ann. Nucl. Energy **13**, 601 (1986).
21. I.A. Korzh, V.A. Mishchenko, N.M. Pravdivy, At. Energ. **62**, 417 (1987).
22. S.F. Hicks, J.R. Vanhoy, A.J. French, S.L. Henderson, T.J. Howard, R.L. Pecha, Z.C. Santonil, B.P. Crider, S. Liu, M.T. McEllistrem, E.E. Peters, F.M. Prados-Estvez, T.J. Ross, S.W. Yates, EPJ Web of Conferences **93**, 02002 (2015).
23. A. Olacel, C. Borcea, P. Dessagne, M. Kerveno, A. Negret, A.J.M. Plompen, Phys. Rev. C **90**, 034603 (2014).
24. M. Nyman, F. Belloni, D. Ichinkhorloo, E. Pirovano, A.J.M. Plompen, C. Rouki, Phys. Rev. C **93**, 024610 (2016).
25. D. Ene, C. Borcea, S. Kopecky, W. Mondelaers, A. Negret, A.J.M. Plompen, Nucl. Instrum. Methods Phys. Res. A **618**, 54 (2010).
26. D. Deleanu, C. Borcea, Ph. Dessagne, M. Kerveno, A. Negret, A.J.M. Plompen, J.C. Thiry, Nucl. Instrum. Methods Phys. Res. **624**, 130 (2010).
27. A. Plompen, N. Nankov, C. Rouki, M. Stanoiu, C. Borcea, D. Deleanu, A. Negret, Ph. Dessagne, M. Kerveno, G. Rudolf, J.C. Thiry, M. Mosconi, R. Nolte, J. Korean Phys. Soc. **59**, 1581 (2011).
28. C.R. Brune, Nucl. Intrum. Methods Phys. Res. A **493**, 106 (2002).
29. A. Olacel, F. Belloni, C. Borcea, M. Boromiza, P. Dessagne, G. Henning, M. Kerveno, A. Negret, M. Nyman, E. Pirovano, A.J.M. Plompen, Phys. Rev. C **96**, 014621 (2018).

30. A.D. Carlson, V.G. Pronyaev, D.L. Smith, N.M. Larson, Z. Chen, G.M. Hale, F.-J. Hambsch, E.V. Gai, S.-Y. Oh, S.A. Badikov, T. Kawano, H.M. Hofmann, H. Vonach, S. Tagesen, Nucl. Data Sheets **110**, 3215 (2009).
31. L.C. Mihailescu, L. Oláh, C. Borcea, A.J.M. Plompen, Nucl. Instrum. Methods Phys. Res. A **531**, 375 (2004).
32. C. Rouki, P. Archier, C. Borcea, C. de Saint Jean, J.C. Droh'e, S. Kopekey, A. Moens, N. Nankov, A. Negret, G. Nogu'ere, A.J.M. Plompen, M. Stanoiu, Nucl. Instrum. Methods Phys. Res. A **672**, 82 (2012).
33. A. Olacel, F. Belloni, C. Borcea, M. Boromiza, Ph. Dessagne, G. Henning, M. Kerveno, A. Negret, M. Nyman, E. Pirovano, A. Plompen, AIP Conf. Proc. **1852**, 080006 (2017).
34. A. Negret, C. Borcea, D. Bucurescu, D. Deleanu, Ph. Dessagne, D. Filipescu, D. Ghita, T. Glodariu, M. Kerveno, N. Marginean, R. Marginean, C. Mihai, S. Pascu, A.J.M. Plompen, T. Sava, L. Stroe, Phys. Rev. C **88**, 034604 (2013).
35. A.J. Koning, S. Hilaire, M.C. Duijvestijn, *TALYS-1.0*, in *Proceedings of the International Conference on Nuclear Data for Science and Technology, April 22-27, 2007, Nice, France*, edited by O. Bersillon, F. Gunsing, E. Bauge, R. Jacqmin, S. Leray (EDP Sciences, 2008) pp. 211–214.
36. E.E. Carroll Jr., G.G. Smith, Nucl. Sci. Eng. **22**, 411 (1965).
37. Chi-Fong Ai, Mien-Win Wu, Jen-Chang Chou, Nucl. Sci. **14**, 1 (1977).
38. Y. Ikeda, C. Konno, K. Kosako, K. Oishi, Japanese report to NEANDC, No. 155, 11 (1990).
39. W. Mannhart, D. Schmidt, AIP Conf. Proc. **769**, 609 (2005).
40. Lu Han-Lin, Li Ji-Zhou, Fan Pei-Guo, Huang Jian-Zhou, Chin. J. Nucl. Phys. **4**, 272 (1982).
41. J.W. Meadows, D.L. Smith, L.R. Greenwood, L.P. Geraldo, W. Mannhart, G. Boerker, G. Mueller, in *Proceedings of the International Conference on Nuclear Data for Science and Technology, May 13-17, 1991, Jülich, Germany* (Springer, 1992).
42. A.J. Koning, J.P. Delaroche, Nucl. Phys. A **713**, 231 (2003).
43. J. Kopecky, M. Uhl, Phys. Rev. C **41**, 1941 (1990).
44. J. Kopecky, M. Uhl, R.E. Chrien, Phys. Rev. C **47**, 312 (1993).
45. D.M. Brink, Nucl. Phys. **4**, 215 (1957).
46. P. Axel, Phys. Rev. **126**, 671 (1962).
47. A. Gilbert, A.G.W. Cameron, Can. J. Phys. **43**, 1446 (1965).
48. A.V. Ignatyuk, G.N. Smirenkin, A.S. Tishin, Sov. J. Nucl. Phys. **21**, 255 (1975).
49. R. Capote, M. Herman, P. Oblozinsky, P.G. Young, S. Goriely, T. Belgya, A.V. Ignatyuk, A.J. Koning, S. Hilaire, V. Plujko, M. Avrigeanu, O. Bersillon, M.B. Chadwick, T. Fukahori, S. Kailas, J. Kopecky, V.M. Maslov, G. Reffo, M. Sin, E. Soukhovitskii, P. Talou, H. Yinlu, G. Zhigang, Nucl. Data Sheets **110**, 3107 (2009).
50. S. Goriely, F. Tondeur, J.M. Pearson, At. Data Nucl. Data Tables **77**, 311 (2001).
51. Yang Dong, Huo Junde, Nucl. Data Sheets **121**, 1 (2014).
52. Phan-Xuan-Ho, J. Bellicard, Ph. Leconte, I. Sick, Nucl. Phys. A **210**, 189 (1973).
53. D.I. Sober, B.C. Metsch, W. Knüpfer, G. Eulenberg, G. Küchler, A. Richter, E. Spamer, W. Steffen, Phys. Rev. C **31**, 6 (1985).
54. T. Lönnroth, J. Hattula, V. Koponen, E.K. Warburton, Phys. Scr. **34**, 669 (1986).
55. M. Dupuis, T. Kawano, J.-P. Delaroche, E. Bauge, Phys. Rev. C **83**, 014602 (2011).
56. T. Kawano, P. Talou, H.A. Weidenmüller, Phys. Rev. C **92**, 044617 (2015).
57. T. Kawano, R. Capote, S. Hilaire, P. Chau Huu-Tai, Phys. Rev. C **94**, 014612 (2016).
58. E.K. Warburton, D.E. Alburger, Phys. Rev. C **6**, 4 (1972).
59. D.A. Brown, M.B. Chadwick, R. Capote, A.C. Kahler, A. Trkov, M.W. Herman, A.A. Sonzogni, Y. Danon, A.D. Carlson, M. Dunn, D.L. Smith, G.M. Hale, G. Arbanas, R. Arcilla, C.R. Bates, B. Beck, B. Becker, F. Brown, R.J. Casperson, J. Conlin, D.E. Cullen, M.-A. Descalle, R. Firestone, T. Gaines, K.H. Guber, A.I. Hawari, J. Holmes, T.D. Johnson, T. Kawano, B.C. Kiedrowski, A.J. Koning, S. Kopecky, L. Leal, J.P. Lestone, C. Lubitz, J.I. Marquez Damian, C.M. Mattoon, E.A. McCutchan, S. Mughabghab, P. Navratil, D. Neudecker, G.P.A. Nobre, G. Noguere, M. Paris, M.T. Pigni, A.J. Plompen, B. Pritychenko, V.G. Pronyaev, D. Roubtsov, D. Rochman, P. Romano, P. Schillebeeckx, S. Simakov, M. Sin, I. Sirakov, B. Sleaford, V. Sobes, E.S. Soukhovitskii, I. Stetcu, P. Talou, I. Thompson, S. van der Marck, L. Welser-Sherrill, D. Wiarda, M. White, J.L. Wormald, R.Q. Wright, M. Zerkle, G. Zerovnik, Y. Zhu, Nucl. Data Sheets **148**, 1 (2018).
60. D. Rochman, A.J. Koning, J.Ch. Sublet, M. Fleming, E. Bauge, S. Hilaire, P. Romain, B. Morillon, H. Duarte, S. Goriely, S.C. van der Marck, H. Sjstrand, S. Pomp, N. Dzysiuk, O. Cabellos, H. Ferroukhi, A. Vasiliev, EPJ Web of Conferences **146**, 02006 (2017).
61. Z.G. Ge, Z.X. Zhao, H.H. Xia, Y.X. Zhuang, T.J. Liu, J.S. Zhang, H.C. Wu, J. Korean Phys. Soc. **59**, 1052 (2011).
62. K. Shibata, O. Iwamoto, T. Nakagawa, N. Iwamoto, A. Ichihara, S. Kunieda, S. Chiba, K. Furutaka, N. Otuka, T. Ohsawa, T. Murata, H. Matsunobu, A. Zukeran, S. Kamada, J. Katakura, J. Nucl. Sci. Technol. **48**, 1 (2011).
63. A. Santamarina, D. Bernard, Y. Rugama, JEFF Report 22 (2009).
64. S.V. Zabrodskaya, A.V. Ignatyuk, V.N. Koshcheev, V.N. Manochin, M.N. Nikolaev, V.G. Pronyaev, Voprosy Atomnoj Nauki i Techniki, Seriya Nuclear Constants Vols. **1-2** (ROSFOND, 2007) p. 3.
65. C.M. Perey, F.G. Perey, At. Data Nucl. data Tables **17**, 1 (1976).
66. R. Capote, K.I. Zolotarev, V.G. Pronyaev, A. Trkov, J. ASTM Int. **9**, 1 (2012).
67. E.M. Zsolnay, R. Capote, H.K. Nolthenius, A. Trkov, Technical report INDC(NDS)-0616 (IAEA, Vienna, 2012).
68. E.M. Cornelis, L. Mewissen, F. Poortmans, in *Proceedings of the International Conference on Nuclear Data for Science and Technology, September 6-10, 1982, Antwerp, Belgium* (Springer, 1983).
69. R.F. Carlton, J.A. Harvey, B. Castel, Bull. Am. Phys. Soc. **30**, 1252 (1985).
70. P. Boschung, J.T. Lindow, E.F. Shrader, Nucl. Phys. A **161**, 593 (1971).
71. W.E. Kinney, F.G. Perey, Oak Ridge National Lab. Reports, No. 4907 (1974).
72. I.A. Korzh, V.A. Mishchenko, E.N. Mozhzhukhin, N.M. Pravdivij, I.E. Sanzhur, Ukr. Fiz. Zh. **22**, 87 (1977).

73. S.M. El-Kadi, C.E. Nelson, F.O. Purser, R.L. Walter, A. Beyerle, C.R. Gould, L.W. Seagondollar, Nucl. Phys. A **390**, 509 (1982).
74. I.A. Korzh, V.A. Mishchenko, N.M. Pravdivy, At. Energ. **62**, 417 (1987).
75. J.R. Vanhoy, S.H. Liu, S.F. Hicks, B.M. Combs, B.P. Crider, A.J. French, E.A. Garza, T. Harrison, S.L. Henderson, T.J. Howard, M.T. McEllistrem, S. Nigam, R.L. Pecha, E.E. Peters, F.M. Prados-Estévez, A.P.D. Ramirez, B.G. Rice, T.J. Ross, Z.C. Santonil, L.C. Sidwell, J.L. Steves, B.K. Thompson, S.W. Yates, Nucl. Phys. **972**, 107 (2018).
76. Rui Li, Weili Sun, E.Sh. Soukhovitskiĩ, J.M. Quesada, R. Capote, Phys. Rev. C **87**, 0546111 (2013).
77. W. Sun, R. Li, E.Sh. Soukhovitskiĩ, J.M. Quesada, R. Capote, Nucl. Data Sheets **118**, 191 (2014).
78. T. Kawano, F.H. Fröhner, Nucl. Sci. Eng. **127**, 130 (1997).
79. Roland Beyer, Arnd R. Junghans, Peter Schillebeeckx, Ivan Sirakov, Tae-Yung Song, Daniel Bemmerer, Roberto Capote, Anna Ferrari, Andreas Hartmann, Roland Hannaske, Jan Heyse, Hyeon Il Kim, Jong Woon Kim, Toni Kögler, Cheol Woo Lee, Young-Ouk Lee, Ralph Massarczyk, Stefan E. Müller, Tobias P. Reinhardt, Marko Röder, Konrad Schmidt, Ronald Schwengner, Tamás Szücs, Marcell P. Takács, Andreas Wagner, Louis Wagner, Sung-Chul Yang, Eur. Phys. J. A **54**, 81 (2018).